RSC Advances

PAPER

View Article Online
View Journal | View Issue

Check for updates

Cite this: *RSC Adv.*, 2020, **10**, 14471

Enhancing cellular morphological changes and ablation of cancer cells *via* the interaction of drug co-loaded magnetic nanosystems in weak rotating magnetic fields

Tingting Wu, †[ab] Qian Zhang,†[c] Huiping Hu,[d] Fang Yang,[e] Ke Li,[a] Yu Zhang[a] and Chen Shi*[ab]

Magnetic nanoparticles have been widely used in cancer treatment for their potential magnetic functions and synergistic antitumor effect with therapeutic agents. In this work, we developed a polymeric nanosystem by co-loading the natural anticancer drug tetrandrine and superparamagnetic iron oxide nanoparticles for cancer combinatorial therapy. The nanosystem possessed regular morphology and superior magnetic properties. Under the action of external rotating permanent magnets, the nanosystem could transfer a rotational motion to damage the cellular membrane, which would result in the increased permeabilization of the cell membrane and damage to lysosomes. Hence, the specific characteristics of the magnetic nanosystem induced potent cytotoxicity and enhanced the effect of the tetrandrine-induced cell apoptosis. With further exploration, we found that this nanoplatform caused cell death *via* a lysosomal-mitochondrial apoptotic pathway with the upregulation of proapoptotic proteins (Cathepsin B, Smac/Diablo, Cytochrome C, and Caspase 3) and the down-regulation of antiapoptotic proteins (Bcl-2 and XIAP). These findings demonstrate that the combination therapy mediated by co-loaded magnetic nanosystems can be used for a multi-therapeutic effect against tumors in biomedical applications.

Received 15th February 2020
Accepted 25th March 2020

DOI: 10.1039/d0ra01458c

rsc.li/rsc-advances

Open Access Article. Published on 16 April 2020. Downloaded on 12/27/2025 3:49:42 AM.
This article is licensed under a Creative Commons Attribution-NonCommercial 3.0 Unported Licence.

1. Introduction

Currently, cancer remains as the leading cause of death and a major threat to public health.[1] Given the complicated etiology and fast progression of cancer, traditional monotherapies, such as chemotherapy, radiotherapy and photo-thermal therapy, are usually sub-effective.[2] Recently, some studies have shown that cancer treatment is much more effective after combining multiple therapeutic modalities compared with monotherapy.[3,4] On the one hand, combination therapy can minimize the required dose for therapeutic agents, thereby reducing the systematic safety concerns. On the other hand, combination therapy can work synergistically to maximize the therapeutic outcomes.[5,6] Therefore, with a rational design, combinatorial therapy would be promising in cancer treatment.

Magnetic nanoparticles can be easily controlled and manipulated by an external magnetic field gradient. In particular, owing to the superparamagnetism, magnetic Fe_3O_4 nanoparticles (MNPs) have attracted much attention as magnetic carriers for targeted drug delivery, magnetic resonance imaging (MRI) for clinical diagnosis, and cancer therapeutic compounds for magnetic hyperthermia.[7–9] Generally, the magnetic heat induction of MNPs is utilized most frequently and has been extensively applied for cancer hyperthermia treatment. However, the heat generated under a high-frequency alternating magnetic field (AMF) cannot be accurately controlled, which may further cause tissue necrosis, especially near thermally sensitive tissues such as the gallbladder, lung or intestine.[10] Compared with the high-frequency AMF, a weak rotating magnetic field (RMF) shows its potential merits in cancer therapy. It has been demonstrated that in the case of low-frequency magnetic fields, the heat generated by MNPs becomes negligible.[11] However, MNPs can produce mechanical forces for movement under a weak RMF or controllable rotation

[a]*Department of Pharmacy, Union Hospital, Tongji Medical College, Huazhong University of Science & Technology (HUST), Wuhan, P. R. China. E-mail: 29136909@qq.com*

[b]*Hubei Province Clinical Research Center for Precision Medicine for Critical Illness, Wuhan 430022, China*

[c]*Key Laboratory for Thin Film and Microfabrication Technology of the Ministry of Education, Department of Instrument Science and Engineering, School of Electronic Information and Electrical Engineering, Institute of Nano Biomedicine and Engineering, Shanghai Jiao Tong University, Shanghai, China*

[d]*Hubei Key Laboratory of Nature Medicinal Chemistry and Resource Evaluation, Tongji Medical College of Huazhong, University of Science and Technology, Wuhan, China*

[e]*Cixi Institute of Biomedical Engineering, CAS Key Laboratory of Magnetic Materials and Devices, Key Laboratory of Additive Manufacturing Materials of Zhejiang Province, Ningbo Institute of Materials Technology and Engineering, Chinese Academy of Sciences, Ningbo 315201, P. R. China*

† These authors contributed equally to this work.

Open Access Article. Published on 16 April 2020. Downloaded on 12/27/2025 3:49:42 AM.
This article is licensed under a Creative Commons Attribution-NonCommercial 3.0 Unported Licence.

speeds, which enhance the cell membrane poration (magnetoporation) as well as injure lysosomal membrane structures and eventually ablate the tumor cells.[12–14] Moreover, RMFs also enhance the release of co-encapsulated drugs when MNPs were co-packed with other therapeutics in a polymeric matrix.[15] Thus, there are potential opportunities for multi-therapeutic modalities when combining RMF treatment with other therapy.

The trend in current cancer treatment is the use of small doses of drugs to achieve a high antitumor effect. However, for most chemotherapeutic agents, poor drug accumulation at the tumor site and drug resistance results in the failure of chemotherapy and cancer reoccurrence.[16,17] Moreover, the high toxicity of anticancer drugs to normal tissues remains a big obstacle, which also restricts the application of antineoplastics.[18,19] It is known that Chinese herbs consist of many active components that have the ability to regulate cell activities.[20] Tetrandrine (Tet), a bisbenzylisoquinoline alkaloid extracted from the root tuber of a medical plant *Stephania tetrandra* S. Moore, is becoming an attractive anticancer candidate due to the obvious toxicity to tumor cells. It can induce direct apoptosis of tumor cells by activating the mitochondrion-mediated apoptotic pathway.[21] In addition, a reversal of multidrug resistance in cancer has been reported recently.[22] However, the practical application of Tet is limited by the poor water-solubility and

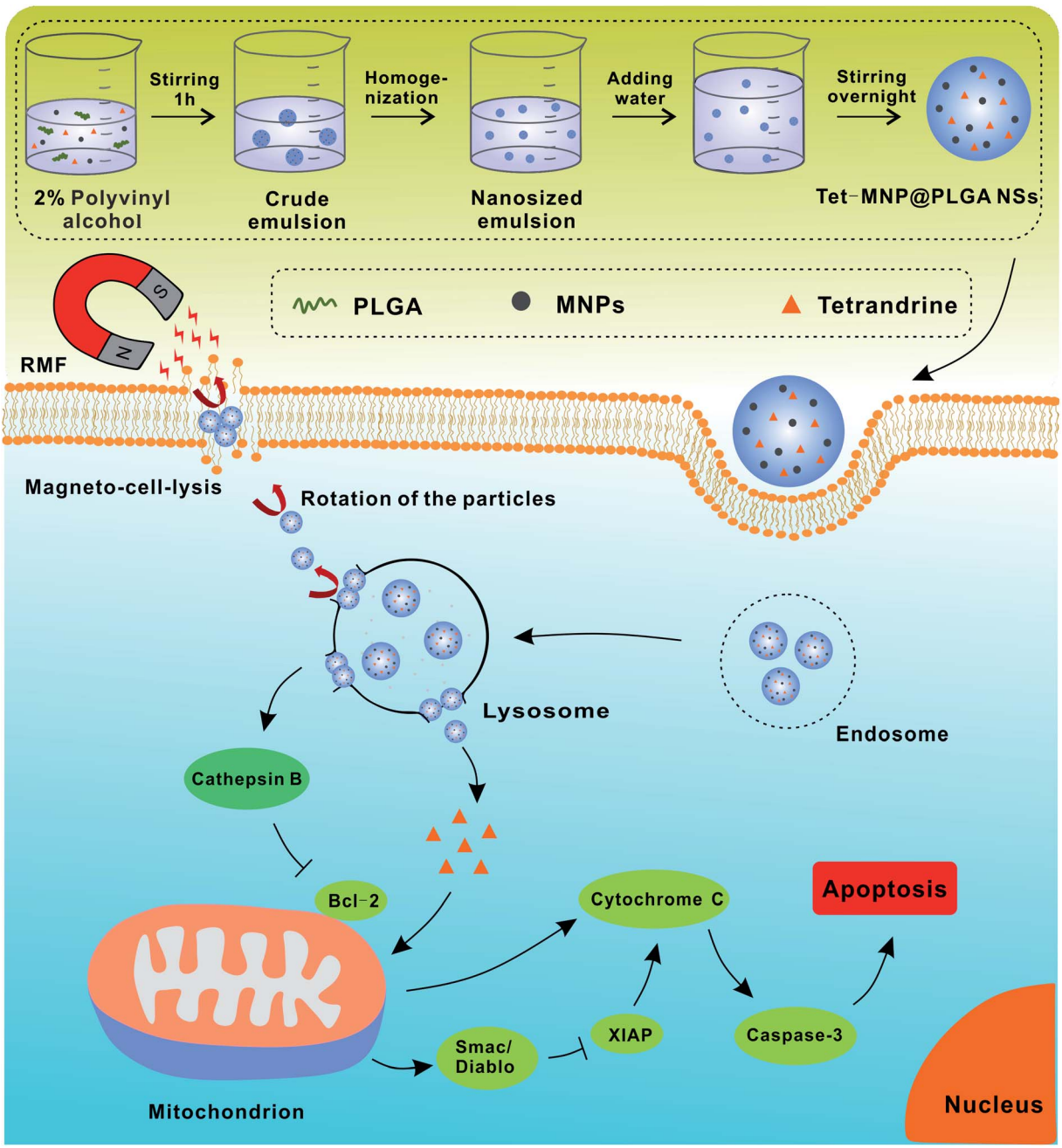

Scheme 1 Schematic illustration of preparation and synergistic antitumor effect of Tet and MNP-co-loaded PLGA nanosystem.

 This journal is © The Royal Society of Chemistry 2020

Open Access Article. Published on 16 April 2020. Downloaded on 12/27/2025 3:49:42 AM.
This article is licensed under a Creative Commons Attribution-NonCommercial 3.0 Unported Licence.

short retention in tumors.[23] To overcome these limitations of Tet and realize its combination with an RMF, we developed poly(lactic-co-glycolic acid) (PLGA) nanosystems (also named Tet-MNP@PLGA NSs) to co-load Tet and MNPs by an emulsion solvent diffusion evaporation method. Lung cancer cell line A549 was chosen as a model to investigate the synergistic antitumor effect of combination therapy. Previously, we demonstrated that Tet-MNP@PLGA NSs can promote the release of Tet from the polymeric matrix under a magnetic field.[24] In this study, we found that with the dual effects of Tet and MNPs, the co-loaded nanosystem induced potent cytotoxicity and serious cell membrane damage to the tumor cells. The nanosystem also increased the membrane permeabilization and injured lysosomes under RMF exposure. A more in-depth exploration of the underlying mechanism of the Tet-MNP@PLGA NS-mediated cell apoptosis *via* lysosomal-mitochondrial apoptotic pathway is shown in Scheme 1. The combinatorial therapy mediated by this multifunctional nanoplatform can be adapted to remotely manipulate other tumor types for effective treatment.

2. Experimental

2.1. Materials and reagents

Iron(III) acetylacetonate, chloroform, oleic acid and oleylamine were purchased from Strem Chemicals, Inc. Postfach, Kehl, Germany. 1,2-Hexadecanediol and benzyl ether were obtained from Sigma-Aldrich, St. Louis, MO, USA. PLGA (Resomer RG 503, MW: 24 000–38 000 Da) was purchased from Evonik Industries, Germany. Tetrandrine (Tet, >98%) was obtained from Wuhan Dinghui Chemical Co., Ltd, China. Polyvinyl alcohol (PVA, Mowiol 4-88) was obtained from Kuraray Specialties Europe GmbH, Frankfurt, Germany. The PromoKine Annexin V-FITC Detection Kit was purchased from PromoCell GmbH, Heidelberg, Germany. BCA protein assay kits were purchased from BioRad, Hercules, USA. The antibodies for Cathepsin B, Bcl-2, Smac/Diablo, XIAP, Cytochrome C, Caspase 3, β-actin and GAPDH were obtained from Cell Signaling Technology, Danvers, MA, USA.

2.2. Cell culture

Human lung cancer A549 cells (ATCC) were used for this study. Cells were grown under standard cell culture conditions in 5% CO_2 at 37 °C to reach a confluence of 70–80% before subjected to any further treatment. All the cells were grown in DMEM medium (Biochrom GmbH, Berlin, Germany) supplemented with 10% fetal bovine serum (PAA laboratories; Cölle, Germany).

2.3. Preparation and characterization of superparamagnetic MNPs

Superparamagnetic MNPs were prepared by following a published procedure reported previously.[25] Briefly, a mixed solvent of oleic acid (6 mmol), oleylamine (6 mmol) and benzyl ether (10 mL) was added in a 100 mL three-neck round bottom flask in the presence of iron(III) acetylacetonate (2 mmol) and 1,2-hexadecanediol (10 mmoL). Under uniform magnetic stirring, the oxygen and moisture in the mixture were first degassed for 30 min at 100 °C. Then, the solution was heated to 200 °C and kept for 2 h under N_2 protection. After refluxing at 300 °C for 1 h, the reaction was stopped and the MNPs were successfully synthesized. Following with centrifugation and precipitation, MNPs were dispersed in ethyl acetate and characterized by transmission electron microscopy (TEM, JOEL model JEM-2010 instrument, JEOL GmbH, Germany).

2.4. Preparation and characterization of Tet-MNPs@PLGA NSs

Tet-MNPs@PLGA NSs were prepared using the emulsion solvent diffusion evaporation method.[26–28] Briefly, PLGA (25 mg mL^{-1}) and Tet (0.5 mg mL^{-1}) were dissolved in 2.5 mL ethyl acetate containing MNPs (20 mg mL^{-1}). This suspension was then added dropwise into 2.5 mL PVA aqueous solution (2%) under stirring. After 1 h, the crude emulsion was homogenized by a ultrasonifier (G560E, Scientific Industries, Inc., USA) and then diluted with deionized water. After stirring overnight to evaporate ethyl acetate, co-loaded nanosystems were collected by centrifugation and resuspended in deionized water. MNP-loaded PLGA nanosystems (MNP@PLGA NSs) were prepared using the same protocol without adding Tet.

The hydrodynamic size and zeta potential of the nanosystem were measured by dynamic light scattering (DLS, Malvern Instruments, UK). The morphology of NPs was visualized by scanning electron microscopy (SEM, JSM-7500F series, JEOL USA, Inc., Peabody, MA, United States) and TEM. The loading of Tet and MNPs in the PLGA were quantified using a UV-visible spectrometer, Multiskan™ GO Microplate Spectrophotometer (Thermo Fischer Scientific, Waltham, MA, United States) and inductively coupled plasma mass spectrometry (ICP-MS, Agilent 7500 Series, Germany), respectively.

2.5. Characterization of the magnetic properties

The samples diluted with deionized water were dropped on austenitic stainless steel and dried at room temperature. Magnetic force microscopy (MFM) was performed using a Nanoscope IV controller (Bruck, Ettlingen, Germany). A magnetized tip (MESP, Bruker, Ettlingen, Germany) was used for recording visual magnetic images.

2.6. Characterization of MNP@PLGA NSs subjected to a magnetic field

SEM imaging was employed to assess the effective dispersion and aggregation of MNP@PLGA NSs in the presence of a RMF. In detail, MNP@PLGA NSs were diluted by demineralized water to the final concentration of 10 μg mL^{-1}. 12 mm cover slips were placed in 30 mm Petri dishes. 300 μL of diluted MNP@PLGA NSs was dropped on the cover slip, exposed to a RMF (1000 rpm) for 40 min, and later allowed to dry at room temperature. The sample was then treated using a Gatan Alto 2500 sputter coater (Alto Cryo-Transfer System ALTO2500, Gatan Inc, Pleasanton, CA, United States) to render the sample conductive. The control

Open Access Article. Published on 16 April 2020. Downloaded on 12/27/2025 3:49:42 AM.
This article is licensed under a Creative Commons Attribution-NonCommercial 3.0 Unported Licence.

group was prepared by the same procedure without being subjected to the RMF.

2.7. Cell viability assay

The *in vitro* dose-dependent activity of the nanosystems was determined by a standard Cell Counting Kit-8 (CCK-8) assay using A549 human lung carcinoma cells. Briefly, cells were seeded in a 96-well plate at a density of 1×10^4 cells per well at 24 h prior to the assay. Then, a series of doses of MNP@PLGA NSs, Tet, and Tet-MNP@PLGA NSs were incubated with the cells. After 8 h incubation, the cell viabilities were detected by CCK-8 assay according to the manufacturer's instruction.

2.8. Study of magneto-cell-lysis

A permanent magnetic stirrer system (magnetic motion Mix 15, 2 mag AG Muenchen, Germany) was employed in the experiments. First, to optimize the rotation speed, the cells were exposed to the RMF treatment for 40 min at different rotation speeds (100, 500, 1000, 1500 rpm). The CCK-8 assay was used to assess the cell viabilities. Thereafter, to evaluate the effect of magneto-cell-lysis, A549 cells were incubated in the presence or absence (as the control group) of 0.25 mg mL^{-1} MNP@PLGA NSs (including 2.78 μg mL^{-1} Fe_3O_4) and 0.25 mg mL^{-1} Tet-MNP@PLGA NSs (including 2.43 μg mL^{-1} Fe_3O_4 and 7.33 μg mL^{-1} Tet) for 7 h. Then, the suspension was removed and the cells were washed three times with PBS to get rid of the extracellular nanoparticles. The cells were then exposed to the RMF (1000 rpm) and measured by the CCK-8 assay to determine the viabilities.

2.9. Apoptosis assay by FACS

The apoptotic death of A549 cells was quantified by flow cytometry with Annexin V-FITC and PI staining. After the treatment of MNP@PLGA NSs and Tet-MNP@PLGA NSs in the presence or absence of the RMF, cells were subjected to Annexin V and PI staining using a PromoKine Annexin V-FITC Detection Kit with the step-by-step protocol provided by the manufacturer and detected by a flow cytometer.

2.10. Monitoring of cellular morphology changes by confocal imaging

PLGA loaded with fluoresceinamine (FA-PLGA) was prepared as a fluorescent nanosystem to evaluate the morphology changes of cells after cellular uptake.[29] A549 cells were seeded onto glass coverslips at a density of 3.0×10^5 cells/mL and then a series of PBS, florescent MNP@PLGA NSs and Tet-MNP@PLGA NSs were co-incubated for 8 h, respectively. Afterwards, the confocal images were recorded by a confocal laser scanning microscope (CLSM 510 Meta, Zeiss) with a Plan Apochromat 63×/1.4 0.1 Oil DIC M27 objective. DAPI stained nuclei was excited with a 405 nm laser diode and the green fluorescence nanosystems were excited at 488 nm. The emission of DAPI was collected using a 420–490 nm band-pass (BP) and the signal of the particles was detected between a 505–545 nm BP.

2.11. Biological SEM imaging of cells

A549 cells were seeded in 10 cm culture dishes and incubated with PBS, MNP@PLGA NSs and Tet-MNP@PLGA NSs in the presence or absence of RMF treatment. Then, the cells were rinsed with cold PBS, harvested by trypsin digestion and observed by SEM (Hitachi, Tokyo, Japan).

2.12. Topography changes of cell membrane

A549 cells were seeded onto glass coverslips at a density of 3.0×10^5 cells per mL. After RMF treatment, cells were fixed with 10% formalin solution. Atomic force microscopy (AFM) was performed using a Nanoscope IV controller (Bruker, Germany). Topological images were recorded in tapping mode using a SNL-10 cantilever (silicon-tip on nitride lever, f_0 = 12–24 kHz, k = 0.06 N m^{-1}, Bruker, Germany). All images were calculated by software Nanoscope analysis 1.4.

2.13. Monitoring the lysosome injuries induced by RMF stimulation

A549 cells were seeded onto glass coverslips at a density of 3.0×10^5 cells per mL. After fluorescent nanosystem and RMF treatment, cells were fixed with 10% formalin solution and then imaged using a confocal laser scanning microscope. DAPI stained nuclei was excited with a 405 nm laser diode and the green fluorescence nanosystems were excited at 488 nm. Finally, the lysosome compartment, which was stained with LysoTracker® Red DND-99 (Invitrogen), was excited at 543 nm using a Helium–Neon laser. The emission of DAPI was collected using a 420–490 nm BP and the signal of the particles was detected between 505–545 nm BP, while the lysotracker was imaged using a 560 nm long-pass.

2.14. Western blotting analysis

A549 cells were treated with PBS, MNP@PLGA NSs and Tet-MNP@PLGA NSs in the presence or absence of the RMF. Then, the cells were collected and lysed with RIPA lysis buffer containing 1 mM phenylmethanesulfonyl fluoride on ice. After centrifugation at 12 000 rpm for 15 min, the total proteins in the collected supernatants were determined by a BCA protein assay kit. The protein samples (20 μg) were then analyzed by western blotting using primary antibodies Cathepsin B, Bcl-2, Smac/Diablo, XIAP, Cytochrome C, Caspase 3, β-actin and GAPDH, followed by peroxidase-conjugated anti-rabbit or anti-mouse secondary antibodies. The protein bands were visualized by ECL (Thermo, USA) using an Automated Imaging System (GeneGnome5, Synoptics Ltd, UK). The quantification of protein bands was completed by ImageJ software (NIH, Maryland, USA).

2.15. Statistical analysis

Results were expressed as mean ± standard deviation. P values for differences were performed using an unpaired, two tailed Student's t-test. The result of $^*p < 0.05$ was considered to be significant. All experiments were conducted independently three times.

 This journal is © The Royal Society of Chemistry 2020

Open Access Article. Published on 16 April 2020. Downloaded on 12/27/2025 3:49:42 AM.
This article is licensed under a Creative Commons Attribution-NonCommercial 3.0 Unported Licence.

3. Results and discussion

3.1. Preparation and characterization of Tet and MNPs co-loaded PLGA nanosystems

MNPs were first prepared as previously reported.[25] According to the TEM results, the MNPs were around 10 nm with regular morphology and good dispersion (Fig. 1A). However, the pure MNPs easily aggregate and can be oxidized owing to the high chemical activity and large ratio of surface area to volume, limiting their use to some extent.[30] A polymeric matrix coating is commonly used to get rid of the drawbacks of MNPs. PLGA, the FDA approved polymer, shows high biocompatibility and

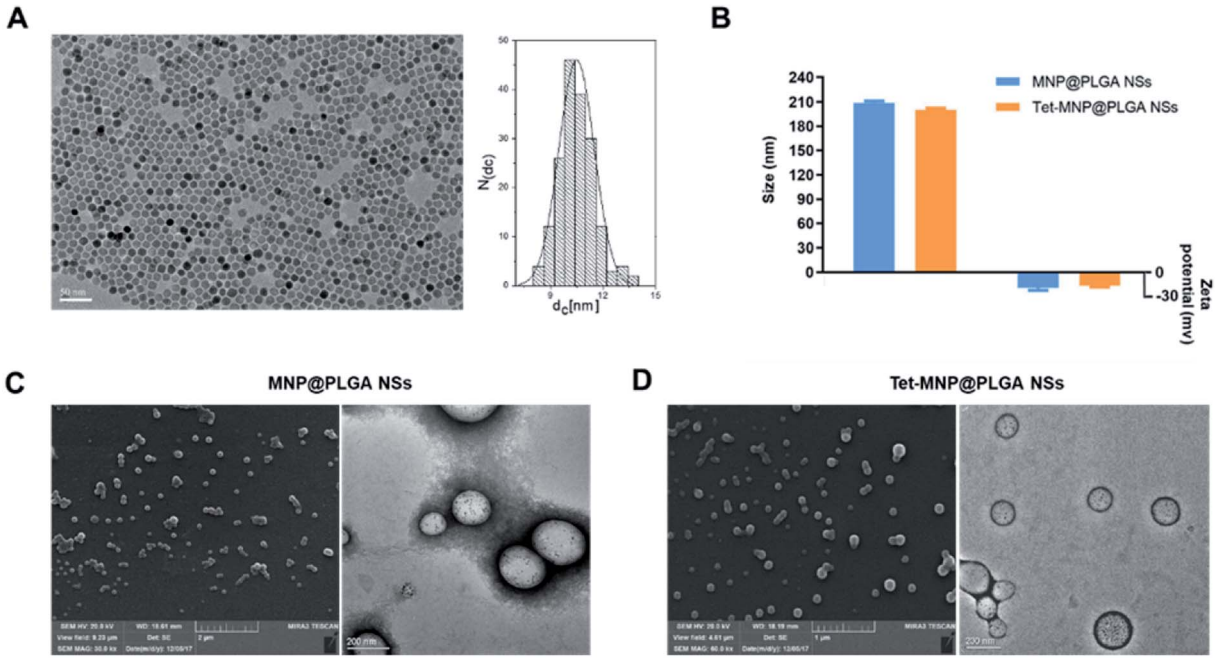

Fig. 1 Preparation and characterization of Tet and MNP co-loaded PLGA nanosystems. (A) TEM image of hydrophobic MNPs with the corresponding diameter histogram made by ImageJ, scale bar = 50 nm. (B) Hydrodynamic size and zeta potential of MNP@PLGA NSs and Tet-MNP@PLGA NSs. (C and D) SEM (left) and TEM (right) images of MNP@PLGA NSs and Tet-MNP@PLGA NSs, respectively.

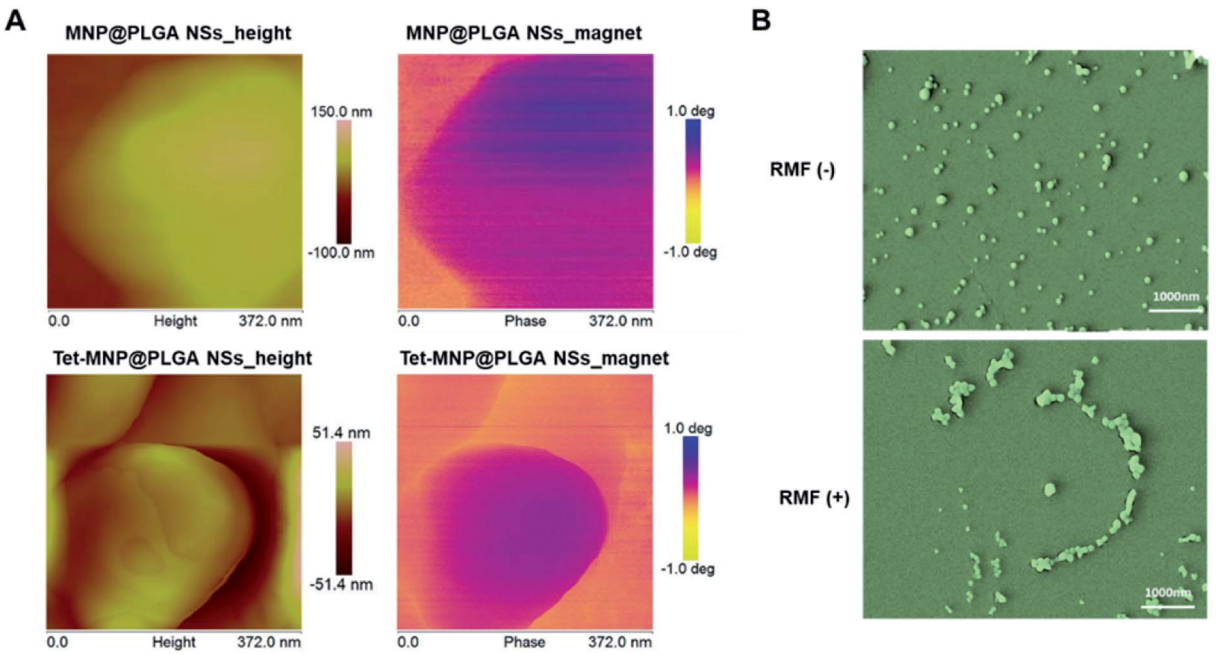

Fig. 2 Characterization of the magnetic properties. (A) Images of MNP@PLGA NSs and Tet-MNP@PLGA NSs observed by AFM and MFM. (B) SEM images of MNP@PLGA NSs in the absence or presence of RMF.

Open Access Article. Published on 16 April 2020. Downloaded on 12/27/2025 3:49:42 AM.
This article is licensed under a Creative Commons Attribution-NonCommercial 3.0 Unported Licence.

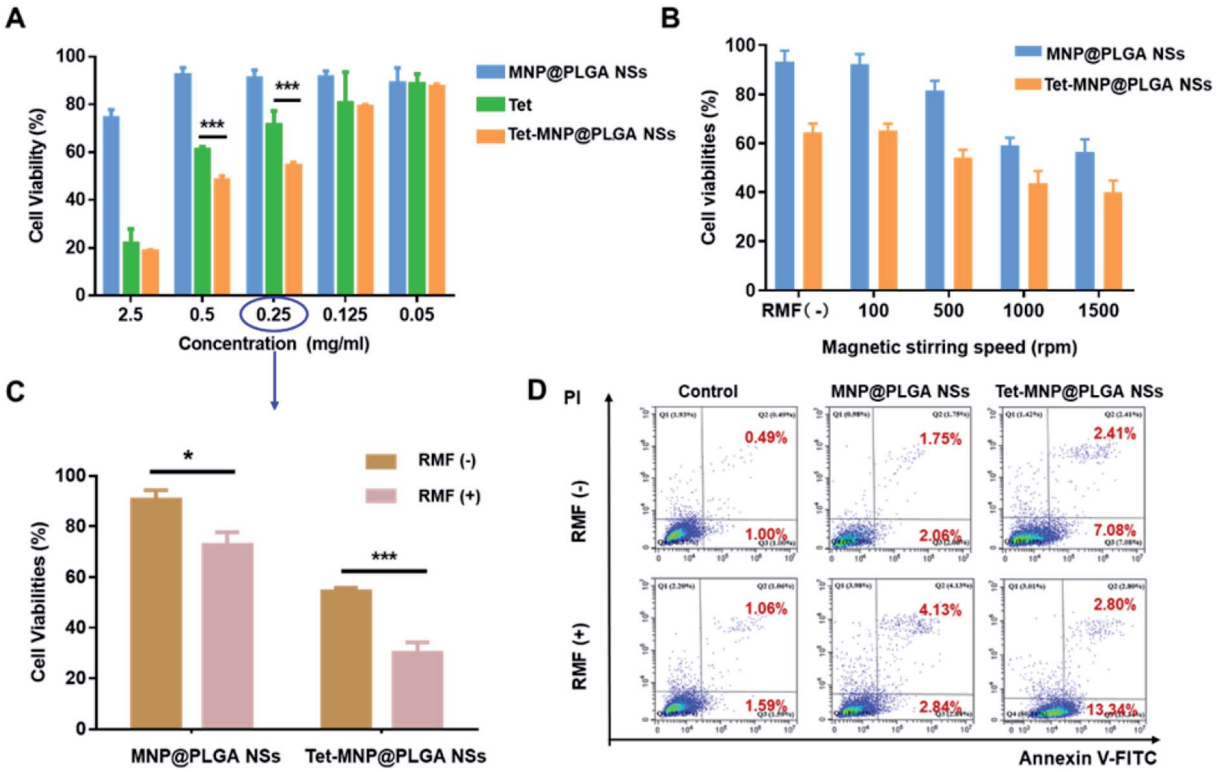

Fig. 3 The cytotoxicity to A549 cells. (A) Dose dependent cell viabilities for A549 cells treated with MNP@PLGA NSs and Tet-MNP@PLGA NSs after 8 h ($n = 5$, ***$p < 0.005$). (B) Cell viabilities for A549 cells treated with MNP@PLGA NSs and Tet-MNP@PLGA NSs after 8 h by different rotating speeds ($n = 5$). (C) Cell viabilities for A549 cells treated with MNP@PLGA NSs and Tet-MNP@PLGA NSs in the presence or absence of the RMF ($n = 5$, *$p < 0.05$, ***$p < 0.005$). (D) Apoptotic rates of A549 cells in the presence or absence of RMF treatment. Q2: necrotic cells; Q3: apoptotic cells; Q4: healthy cells.

biodegradability and has thus been widely used for drug delivery.[31] Moreover, PLGA can easily co-encapsulate the chemically active MNPs and hydrophobic Tet by a facile emulsion solvent diffusion evaporation method, by which MNP@PLGA NSs and Tet-MNP@PLGA NSs were synthesized. Their physical properties were characterized *via* DLS, SEM and TEM, respectively. As shown in Fig. 1B, both MNP@PLGA NSs and Tet-MNP@PLGA NSs showed consistent size ranges around 200 nm and zeta potentials of −20 mV with a narrow size distribution (PDI < 0.1). SEM images revealed spherical nanoparticles and TEM images displayed MNPs that were uniformly dispersed in the polymeric nanoparticles. There was no significant difference in morphology between the MNP@PLGA NSs and Tet-MNP@PLGA NSs, indicating that the Tet loading had a negligible influence on the particle morphology (Fig. 1C and D). Furthermore, the drug loading efficiency (DLE) and encapsulation efficiency (EE) of Tet and MNPs in Tet-MNP@PLGA NSs were determined by UV-visible spectroscopy and ICP-MS. The results showed that 1.42 ± 0.26% of MNPs (EE% as 52.76 ± 3.22%) and 1.79 ± 0.17% of Tet (EE% as 64.54 ± 3.67%) were loaded in Tet-MNP@PLGA NSs. The DLE% and EE% of MNPs in MNP@PLGA NSs were 1.63 ± 0.21% and 59.08 ± 1.44%, respectively. The results indicated that Tet and MNPs can be effectively co-loaded by PLGA nanosystems.

3.2. Characterization of the magnetic properties

MFM was used to investigate the magnetic domain *via* the interactions between a magnetized Cobalt–Chromium tip and the samples. The magnetic MNP@PLGA NSs dropped on austenitic stainless steel easily phase separated under RMF conditions. Herein, the magnetic region can be distinguished from the steel by exhibiting phase contrast. As shown in Fig. 2A, the magnetic region reflected in the phase canal clearly shows the magnetic profile of both MNP@PLGA NSs and Tet-MNP@PLGA NSs, which is attributed to the containment of superparamagnetic MNPs in the polymeric matrix. Most of the regions in the particles showed a uniform color contrast while some regions had a more pronounced contrast than the others. This is probably caused by the fact that some MNPs are shallower inside the polymeric matrix and the shallower ones showed the stronger contrast in the MFM image.[32]

To further evaluate the magnetic properties of MNP@PLGA NSs, the effective dispersion and aggregation of MNP@PLGA NSs were assessed by SEM to identify the RMF effect. The results showed that the incomplete self-rotation and aggregation of magnetic particles can produce a kind of rotational shear force under RMF conditions. However, in the absence of RMF treatment, the nanosystems distributed uniformly in the monitoring horizon (Fig. 2B). Due to the effect of shear forces, we speculated that the rotation effect of magnetic particles could

 This journal is © The Royal Society of Chemistry 2020

Open Access Article. Published on 16 April 2020. Downloaded on 12/27/2025 3:49:42 AM.
This article is licensed under a Creative Commons Attribution-NonCommercial 3.0 Unported Licence.

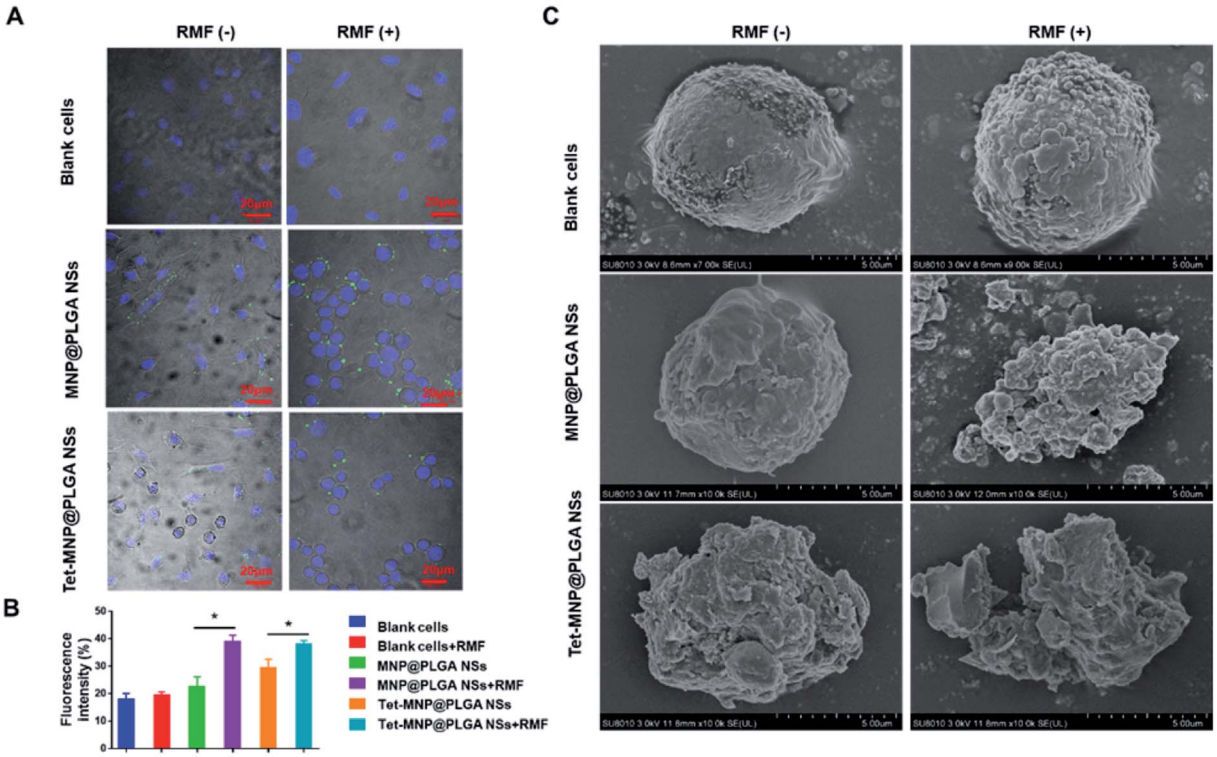

Fig. 4 Morphological characterization of A549 cells by confocal microscopy and biological SEM. (A) A549 cells treated with or without RMF. The green color particles were the fluorescently labeled PLGA NPs (MNP@PLGA NSs and Tet-MNP@PLGA NSs) and cell nuclei were stained with DAPI (blue). Scale bar = 20 μm. (B) Fluorescence intensity quantification of the DAPI stained cells nuclear before and after the RMF treatment ($n = 3$, *$p < 0.05$). (C) Biological SEM images of A549 cells with or without RMF treatment. Scale bar = 5 μm.

increase the cell membrane permeability, especially as they can penetrate the cell membrane when aggregated, leading to the loss of cell viability. To validate this hypothesis, the interaction of the magnetic particles with lung cancer cells A549 was investigated in the subsequent experiments.

3.3. The cytotoxicity to A549 cells

To investigate the cytotoxicity to A549 cells, the cell viabilities were first measured after 8 hours of incubation with various concentrations of free Tet, MNP@PLGA NSs and Tet-MNP@PLGA NSs. The results displayed in Fig. 3A show that all formulations demonstrated a dose-dependent behavior. For the untreated cells, the cell viabilities were 100 ± 1.53%. When at a concentration of 0.05 mg mL^{-1}, all of the three treated groups showed high cell survival rate with approximately 90% cell viability. For MNP@PLGA NSs at 0.125 to 0.5 mg mL^{-1} concentration groups, the formulation was ineffective in reducing the cell viability. Even at a high concentration, *i.e.* 2.5 mg mL^{-1}, the cell viability was 74.36 ± 3.55%. The low toxicity of the MNP@PLGA NSs indicated that this nanosystem could be an ideal carrier for drug delivery. With the concentration increasing from 0.125 to 2.5 mg mL^{-1}, Tet-MNP@PLGA NSs significantly reduced the cell survival from 79.2 ± 0.83% to 18.67 ± 0.56%. Compared with the 0.5 mg mL^{-1} group (48.13 ± 1.87%), 0.25 mg mL^{-1} of Tet-MNP@PLGA NSs (54.56 ± 1.27%) showed slightly increased cell viabilities. Herein, the 0.25 mg mL^{-1} group was chosen for further investigation of the cellular response when subjected to the RMF.

To evaluate the influence of rotation speed, the magnetic stirring speeds were fixed at 100, 500, 1000 and 1500 rpm, respectively. After RMF treatment, the cell viabilities were significantly decreased for both MNP@PLGA NSs and Tet-MNP@PLGA NSs. Modest cell viabilities changed when the rotating speed was fixed at 100 rpm and 500 rpm. When applied to RMF treatment for 40 min at 1000 rpm, the cell viabilities of Tet-MNP@PLGA NSs was approximately 20.71% lower than that without RMF treatment. For MNP@PLGA NSs, the reduction in cell viabilities was around 33.95% (Fig. 3B). When the rotating speed increased from 1000 rpm to 1500 rpm, the cell viability of Tet-MNP@PLGA NSs decreased from 43.71 ± 5.02% to 40.13 ± 4.67%, showing no significant difference. Therefore, the magnetic stirring speeds at 1000 rpm was selected as the rotating speed for further study.

The influence of the RMF on A549 cells was then evaluated. According to the results of the CCK-8 assay, both MNP@PLGA NSs and Tet-MNP@PLGA NSs remarkably reduced the cell viabilities after being subjected to the RMF treatment. Compared with MNP@PLGA NSs, Tet-MNP@PLGA NSs were more effective in inducing cancer cell death, which was attributed to the dual effect of Tet and MNPs (Fig. 3C). Apoptosis is a normal physiological process which occurs during embryonic

Open Access Article. Published on 16 April 2020. Downloaded on 12/27/2025 3:49:42 AM.
This article is licensed under a Creative Commons Attribution-NonCommercial 3.0 Unported Licence.

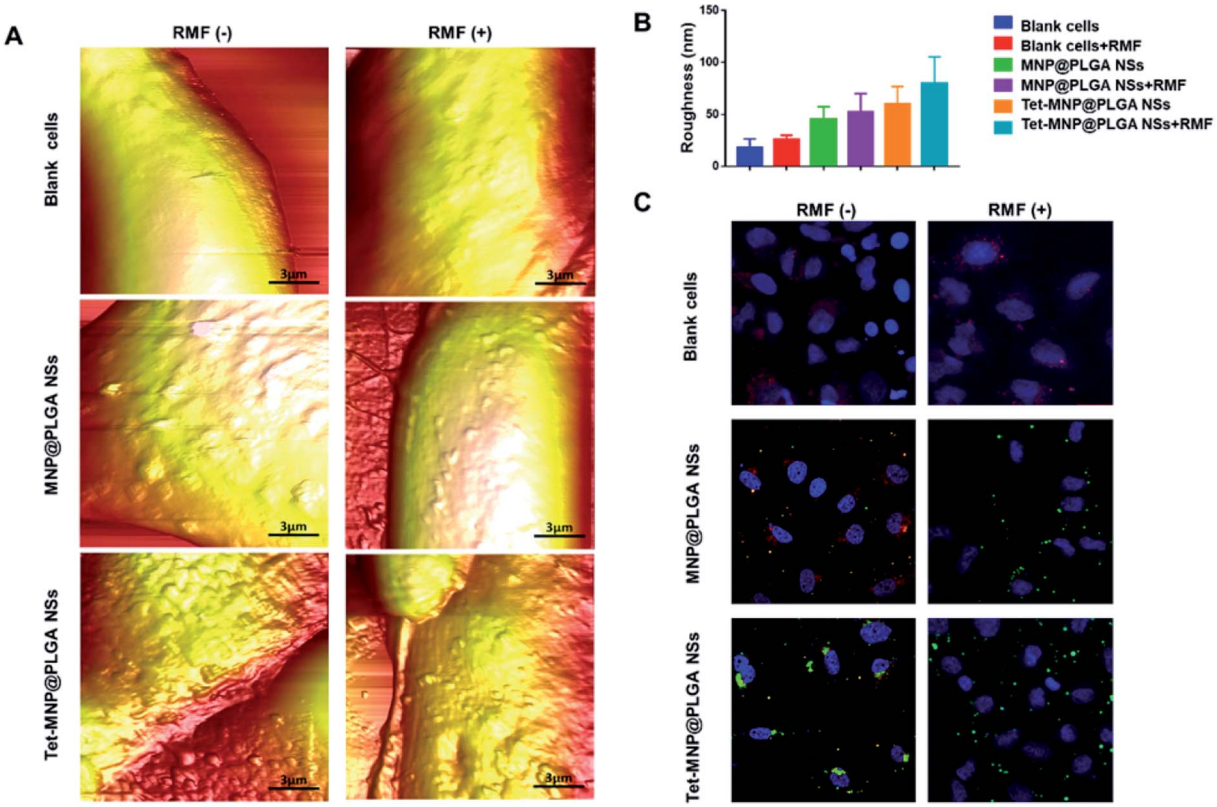

Fig. 5 Cellular mechanism analysis of the magneto-cell-lysis. (A) AFM topography of cell membrane after various treatments. Scale bar = 3 μm. (B) Quantitative analysis of membrane roughness (n = 3). (C) RMF treatment decreased intracellular lysosomes in A549 cells. Lysosomes were stained with LysoTracker® Red DND-99. Scale bar = 20 μm.

development and in the maintenance of tissue homeostasis.[33] We further investigated the cell apoptosis quantitatively by FACS-Annexin V/PI measurements. When apoptosis is measured over time, cells can be tracked from FITC Annexin V and PI negative (Fig. 3D, Q4: viable, or no measurable apoptosis), to FITC Annexin V positive and PI negative (Fig. 3D, Q3: early apoptosis) and finally to FITC Annexin V and PI positive (Fig. 3D, Q2: necrosis, lost membrane integrity). The RMF has no effect on untreated cells. However, when subjected to the RMF, MNP@PLGA NSs increased the cell apoptosis compared to the non-treated group. The evaluation of the number of apoptotic cells for Tet-MNP@PLGA NSs with the RMF showed the highest percentage of apoptosis (about 16.14%) among all groups. These findings indicated that Tet-MNP@PLGA NSs can synergistically enhance Tet-induced cell apoptosis by RMF treatment and hence exhibit the dual anti-tumor effect.

3.4. Morphology characterization of A549 cells with RMF treatment

To observe the morphological changes of A549 cells, fluorescence labeled PLGA NPs (MNP@PLGA NSs and Tet-MNP@PLGA NSs) were incubated with A549 cells, respectively. The RMF was applied for 40 min at a rotating speed of 1000 rpm. Then, the cells were stained with the nuclear marker DAPI and imaged by confocal microscopy. As shown in Fig. 4A, A549 cells kept the typical stretched, shuttle type morphology. The cells morphology changed from healthy shuttle type to the spherical shape when A549 cells were incubated with MNP@PLGA NSs and subjected to the RMF. For Tet-MNP@PLGA NSs without RMF, either the normal cells or dead cells could be observed. This may be due to the release of Tet induced cell death. In addition, after RMF treatment, a significant morphology change was observed in that almost all the cells were spherical. Furthermore, a re-distribution of MNP@PLGA NSs or Tet-MNP@PLGA NSs in the cells was observed after being subjected to the RMF; the uniformly dispersed NPs were gathered around the cell membrane. We further quantitatively analyzed the fluorescence intensity change of DAPI before and after the RMF treatment. As shown in Fig. 4B, the RMF treatment had no effect on the blank cells. Prior to the RMF treatment, no difference in fluorescence intensity was found between the blank cells and MNP@PLGA NS treated cells. In contrast to cells incubated with MNP@PLGA NSs and Tet-MNP@PLGA NSs, RMF treatments of the two groups led to increased fluorescence intensities of 16.42% and 8.73%, respectively, which could be attributed to the magnetic effect that facilitated cell apoptosis.

Biological SEM was then employed to monitor the cell membrane damage after various treatments. As Fig. 4C shows, the blank cells had regular and intact morphology with or without the RMF. In the absence of the RMF, MNP@PLGA NSs

 This journal is © The Royal Society of Chemistry 2020

Open Access Article. Published on 16 April 2020. Downloaded on 12/27/2025 3:49:42 AM.
This article is licensed under a Creative Commons Attribution-NonCommercial 3.0 Unported Licence.

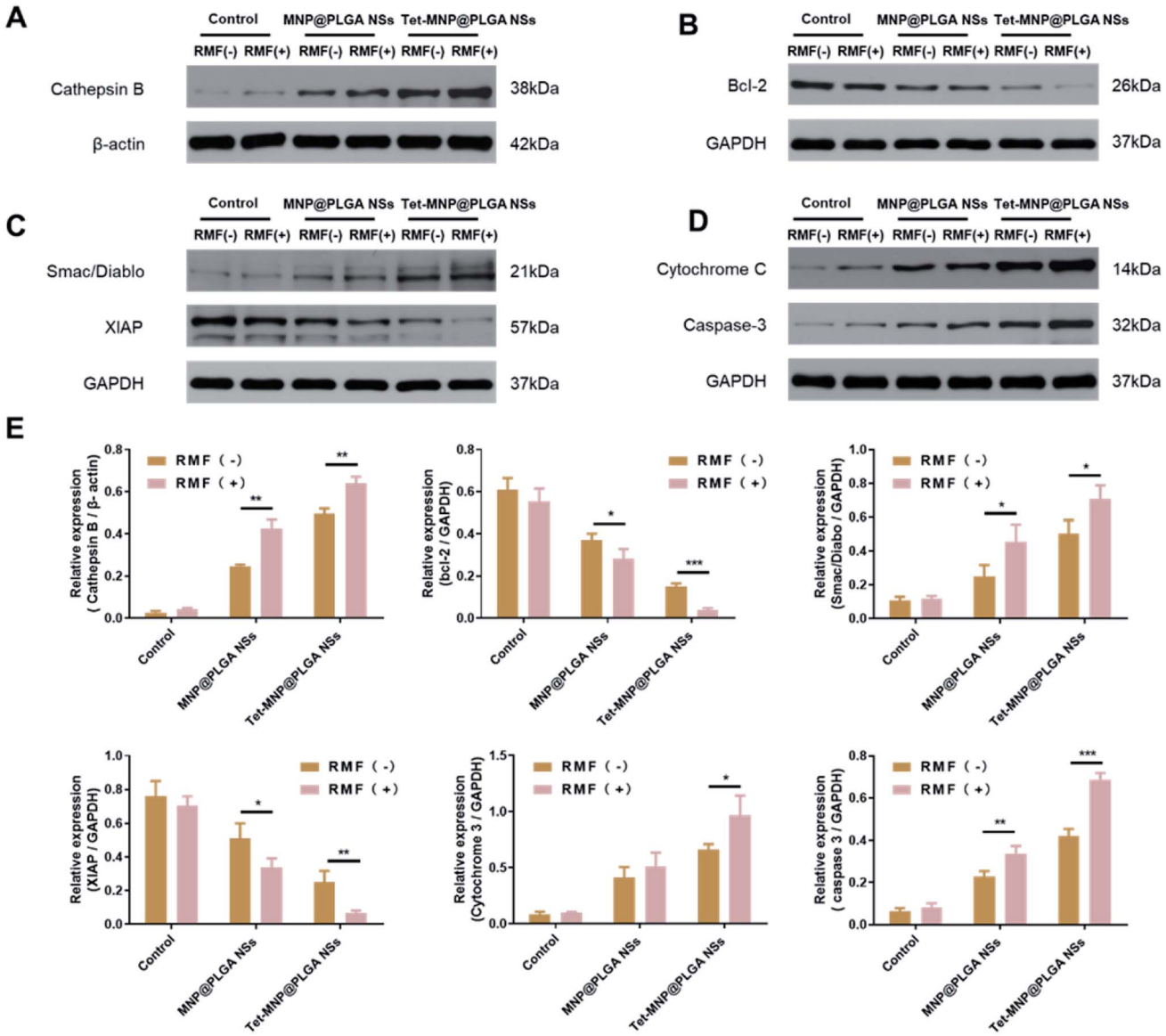

Fig. 6 Study of molecular mechanism of cell apoptosis. (A) Western blotting analysis of Cathepsin B. (B) Western blotting analysis of Bcl-2. (C) Western blotting analysis of Smac/Diablo and XIAP. (D) Western blotting analysis of Cytochrome C and Caspase 3. (E) Quantitative analysis of protein bands ($n = 3$, $^{*}p < 0.05$, $^{**}p < 0.01$, $^{***}p < 0.005$).

exhibited a negligible influence on A549 cells. When subjected to the RMF, the membranes of MNP@PLGA NS-treated cells were seriously disrupted. The cell membranes in the Tet-MNP@PLGA NS-treated group without the RFM were also damaged to some extent. Notably, Tet-MNP@PLGA NSs with RMF treatment caused serious damage to the cellular morphology, which could be attributed to the synergistic effect of Tet and magneto-cell-lysis.[34]

3.5. Study of cellular mechanism of the magneto-cell-lysis

We have demonstrated that the magnetic nanosystems can cause cell morphology changes and membrane damage under RMF conditions. To explore the underlying mechanism, *in situ* AFM was first applied to investigate the harmful effects of the multifunctional nanosystems. The effects were identified by comparing the sample topology and analyzing the cell surface roughness. According to the morphological description in Fig. 5A, MNP@PLGA NSs showed rougher surfaces than the blank cells, which was attributed to the nanoparticles on or beneath the cell surface. After magnetic stirring (1000 rpm for 40 min), the membrane roughness of MNP@PLGA NS treated cells was increased. Compared with the other groups, cells treated with Tet-MNP@PLGA NSs + RMF exhibited rougher membrane surfaces and less regular structures, which was due to the rotational movement of the particles. In addition, a roughness analysis of the AFM micrographs quantitatively supported the morphological changes of the cell membrane. As shown in Fig. 5B, the membrane roughness (calculated 10 times in an area of 3×3 μm^2 of each image) showed a significant

Open Access Article. Published on 16 April 2020. Downloaded on 12/27/2025 3:49:42 AM.
This article is licensed under a Creative Commons Attribution-NonCommercial 3.0 Unported Licence.

increase by the Tet-MNP@PLGA NSs with RMF treatment in comparison to the untreated cells.

It is known that nanoparticles enter into lysosomes after being incorporated in the cells.[35] To further understand the cell apoptosis mechanism caused by the magneto-cell-lysis, we investigated the potential to injure lysosomes by the RMF treatment *via* MNP@PLGA NSs or Tet-MNP@PLGA NSs. The disruption of the lysosomes was determined by monitoring the fluorescence intensity changes of LysoTracker Red. As Fig. 5C shows, the RMF treatment had no effect on the blank cell groups with no obvious fluorescence changes. For the MNP@PLGA NSs without RMF treatment, the stained lysosome had a clear color, indicating that the lysosome was intact and normal. When the RMF is applied, the mechanical force produced by rotation can injure the lysosome and the pH of the lysosomal environment would increase, which would cause the fluorescence intensity of the dye to decrease or even disappear. As Tet itself can destroy the lysosome, the fluorescence intensity was also reduced after the Tet-MNP@PLGA NSs treatment. When further exposed to the RMF, Tet and magnetic movement had a dual effect in destroying the lysosome. Accordingly, with lysosomal disruption, the green fluorescence of the nanosystems was found to be distributed uniformly in the cytoplasm.

3.6. Study of molecular mechanism of cell apoptosis

As described above, the formulated magnetic nanosystems can remarkably reduce the cell viabilities by disrupting the cell membrane and injuring the lysosomes of tumor cells under RMF treatment. To explore the molecular mechanism for cell apoptosis, A549 cells with various treatments were lysed and prepared for western blotting analysis. Cathepsins are a group of cysteine proteases that are largely found in lysosomes. Many stimuli can directly or indirectly induce lysosomal permeabilization and promote the release of cysteine cathepsins into the cytosol.[36] The extracted cathepsins can further cleave the anti-apoptotic Bcl-2 family Bid and induce the intrinsic pathway of apoptosis, involving the release of Cytochrome C from mitochondria and activation of Caspase-3.[37] Moreover, upon apoptotic stimuli, mitochondria are able to release Smac/Diblo, a proapoptotic protein, to the cytosol. Smac/Diablo can then interact with the inhibitor of apoptosis (IAP), blocking the inhibition of IAP to Caspases mediated cell apoptosis.[38] In this experiment, the expression of Cathepsin B in MNP@PLGA NS and Tet-MNP@PLGA NS treated cells was significantly increased by RMF treatment, while the expression of Bcl-2 was decreased accordingly compared to cells without RMF treatment (Fig. 6A and B). In addition, Smac/Diablo was enhanced, whereas XIAP was reduced by RMF treatment (Fig. 6C). The levels of Cytochrome C and Caspase-3 were then up-regulated, triggering the apoptosis of cancer cells (Fig. 6D). Notably, Tet-MNP@PLGA NSs with RMF treatment showed the most potent ability in increasing the proapototic proteins as well as decreasing the antiapoptotic proteins among all groups, demonstrating the synergistic effect of Tet and RMF for apoptosis. Moreover, these proteins were quantitatively analyzed by ImageJ software, which was in good agreement with the protein bands (Fig. 6E). Collectively, these results indicated that the co-loaded magnetic nanosystems induced cell death *via* a lysosomal-mitochondrial apoptotic pathway.

4. Conclusion

In conclusion, we developed a PLGA-based multifunctional nanosystem by co-loading Tet and MNPs. The formulated Tet-MNP@PLGA NSs maintained the good magnetic properties of the MNPs. Under RMF exposure, Tet-MNP@PLGA NSs damaged the cell membrane and injured the lysosome, exhibiting a synergistic effect with Tet. With the dual apoptotic effect of Tet and MNPs, this nanoplatform showed high antitumor efficiency against A549 cells. Therefore, the co-loaded magnetic nanosystems are promising in combination therapy and possess great potential in the treatment of multiple cancer types.

Conflicts of interest

There are no conflicts to declare.

Acknowledgements

This work was financially supported by the National Natural Science Foundation of China (#81603037), Natural Science Foundation of Hubei Province (#2019CFB490) and, Shanghai Sailing Program (No. 19YF1422300).

References

1 R. L. Siegel, K. D. Miller and A. Jemal, *Ca-Cancer J. Clin.*, 2019, **69**, 7–34.
2 W. Dai, X. Wang, G. Song, T. Liu, B. He, H. Zhang, X. Wang and Q. Zhang, *Adv. Drug Delivery Rev.*, 2017, **115**, 23–45.
3 W. Chen, K. Zeng, H. Liu, J. Ouyang, L. Wang, Y. Liu, H. Wang, L. Deng and Y. N. Liu, *Adv. Funct. Mater.*, 2017, **27**, 1605795.
4 C. Chu, E. Ren, Y. Zhang, J. Yu, H. Lin, X. Pang, Y. Zhang, H. Liu, Z. Qin and Y. Cheng, *Angew. Chem.*, 2019, **131**, 275–278.
5 H. Ledford, *Nature*, 2016, **532**, 162–164.
6 S. Mignani, M. Bryszewska, B. Klajnert-Maculewicz, M. Zablocka and J.-P. Majoral, *Biomacromolecules*, 2015, **16**, 1–27.
7 R. A. Revia and M. Zhang, *Mater. Today*, 2016, **19**, 157–168.
8 S. Durr, C. Janko, S. Lyer, P. Tripal, M. Schwarz, J. Zaloga, R. Tietze and C. Alexiou, *Nanotechnol. Rev.*, 2013, **2**, 395–409.
9 N. Lee, D. Yoo, D. Ling, M. H. Cho, T. Hyeon and J. Cheon, *Chem. Rev.*, 2015, **115**, 10637–10689.
10 J. You, R. Zhang, C. Y. Xiong, M. Zhong, M. Melancon, S. Gupta, A. M. Nick, A. K. Sood and C. Li, *Cancer Res.*, 2012, **72**, 4777–4786.
11 D. W. Wong, W. L. Gan, Y. K. Teo and W. S. Lew, *Cell Death Discovery*, 2018, **4**, 49.
12 J. L. Corchero and A. Villaverde, *Trends Biotechnol.*, 2009, **27**, 468–476.

 This journal is © The Royal Society of Chemistry 2020

Open Access Article. Published on 16 April 2020. Downloaded on 12/27/2025 3:49:42 AM.
This article is licensed under a Creative Commons Attribution-NonCommercial 3.0 Unported Licence.

13 V. Pensabene, O. Vittorio, V. Raffa, A. Ziaei, A. Menciassi and P. Dario, *IEEE Transactions on NanoBioscience*, 2008, **7**, 105–110.
14 D. Liu, L. Wang, Z. Wang and A. Cuschieri, *Nano Lett.*, 2012, **12**, 5117–5121.
15 G. Podaru, S. Ogden, A. Baxter, T. Shrestha, S. Ren, P. Thapa, R. K. Dani, H. Wang, M. T. Basel, P. Prakash, S. H. Bossmann and V. Chikan, *J. Phys. Chem. B*, 2014, **118**, 11715–11722.
16 M. M. Gottesman, T. Fojo and S. E. Bates, *Nat. Rev. Cancer*, 2002, **2**, 48.
17 A. M. Calcagno, C. D. Salcido, J. P. Gillet, C. P. Wu, J. M. Fostel, M. D. Mumau, M. M. Gottesman, L. Varticovski and S. V. Ambudkar, *J. Natl. Cancer Inst.*, 2010, **102**, 1637–1652.
18 D. L. Rayle and R. E. Cleland, *Plant Physiol.*, 1992, **99**, 1271–1274.
19 L. Wang, H. Zhang, B. Chen, G. Xia, S. Wang, J. Cheng, Z. Shao, C. Gao, W. Bao, L. Tian, Y. Ren, P. Xu, X. Cai, R. Liu and X. Wang, *Int. J. Nanomed.*, 2012, **7**, 789–798.
20 P. G. Bradford and A. B. Awad, *Mol. Nutr. Food Res.*, 2007, **51**, 161–170.
21 R. Qin, H. Shen, Y. Cao, Y. Fang, H. Li, Q. Chen and W. Xu, *PLoS One*, 2013, **8**, e76486.
22 Z. L. Liu, T. Hirano, S. Tanaka, K. Onda and K. Oka, *J. Pharm. Pharmacol.*, 2003, **55**, 1531–1537.
23 K. F. Guo and J. Cang, *Lett. Drug Des. Discovery*, 2017, **14**, 686–689.
24 C. Shi, C. Thum, Q. Zhang, W. Tu, B. Pelaz, W. J. Parak, Y. Zhang and M. Schneider, *J. Controlled Release*, 2016, **237**, 50–60.
25 S. Sun, H. Zeng, D. B. Robinson, S. Raoux, P. M. Rice, S. X. Wang and G. Li, *J. Am. Chem. Soc.*, 2004, **126**, 273–279.
26 N. Nafee, M. Schneider, K. Friebel, M. Dong, U. Schaefer, T. Mürdter and C.-M. Lehr, *Eur. J. Pharm. Biopharm.*, 2012, **80**, 478–489.
27 R. Dinarvand, N. Sepehri, S. Manoochehri, H. Rouhani and F. Atyabi, *Int. J. Nanomed.*, 2011, **6**, 877–895.
28 K. Wang, H. Hu, Q. Zhang, Y. Zhang and C. Shi, *J. Microencapsulation*, 2019, **36**, 356–370.
29 E. Horisawa, K. Kubota, I. Tuboi, K. Sato, H. Yamamoto, H. Takeuchi and Y. Kawashima, *Pharm. Res.*, 2002, **19**, 132–139.
30 H. Zhang, X. Zhong, J. J. Xu and H. Y. Chen, *Langmuir*, 2008, **24**, 13748–13752.
31 D. Ding and Q. Zhu, *Mater. Sci. Eng., C*, 2018, **92**, 1041–1060.
32 D. A. Bizyaev, A. A. Bukharaev, R. I. Khaibullin, N. M. Lyadov and I. M. Doludenko, *Russ. Microelectron.*, 2018, **47**, 187–196.
33 A. Sasnauskiene, J. Kadziauskas, N. Vezelyte, V. Jonusiene and V. Kirveliene, *Apoptosis*, 2009, **14**, 276–286.
34 S. H. Hu and X. Gao, *J. Am. Chem. Soc.*, 2010, **132**, 7234–7237.
35 M.-T. Gyparaki and A. G. Papavassiliou, *Trends Mol. Med.*, 2014, **20**, 239–241.
36 V. Stoka, V. Turk and B. Turk, *Biol. Chem.*, 2007, **388**, 555–560.
37 V. Stoka, B. Turk, S. L. Schendel, T.-H. Kim, T. Cirman, S. J. Snipas, L. M. Ellerby, D. Bredesen, H. Freeze and M. J. Abrahamson, *J. Biol. Chem.*, 2001, **276**, 3149–3157.
38 C. Du, M. Fang, Y. Li, L. Li and X. Wang, *Cell*, 2000, **102**, 33–42.